Rock Mech Rock Eng (2016) 49:1611–1627
DOI 10.1007/s00603-015-0867-y

ORIGINAL PAPER

The 3D Numerical Simulation for the Propagation Process of Multiple Pre-existing Flaws in Rock-Like Materials Subjected to Biaxial Compressive Loads

J. Bi[1,2] · X. P. Zhou[1,2,3] · Q. H. Qian[3]

Received: 16 March 2015 / Accepted: 1 October 2015 / Published online: 12 October 2015
© Springer-Verlag Wien 2015

Abstract General particle dynamics (GPD), which is a novel meshless numerical method, is proposed to simulate the initiation, propagation and coalescence of 3D pre-existing penetrating and embedded flaws under biaxial compression. The failure process for rock-like materials subjected to biaxial compressive loads is investigated using the numerical code GPD3D. Moreover, internal crack evolution processes are successfully simulated using GPD3D. With increasing lateral stress, the secondary cracks keep growing in the samples, while the growth of the wing cracks is restrained. The samples are mainly split into fragments in a shear failure mode under biaxial compression, which is different from the splitting failure of the samples subjected to uniaxial compression. For specimens with macroscopic pre-existing flaws, the simulated types of cracks, the simulated coalescence types and the simulated failure modes are in good agreement with the experimental results.

Keywords General particle dynamics (GPD) · Propagation of 3D cracks · Coalescence of 3D cracks · Biaxial compression · 3D numerical simulation

Abbreviations

D	A disturbance coefficient
E	Young's modulus
f	Interaction factor
D_1	Damage factor
G	Shear modulus
U	Undamaged particles
D_a	Damaged particles
h	Smoothing length
μ	Poisson ratio
ρ	Real time mass density
ρ_0	The initial density
k	The modulus of volume elasticity
v_i	Particle velocity at ith particle
$\dot{R}^{\alpha\beta}$	Rotation rate
x^{α}	Spatial coordinate (X)
$\dot{\varepsilon}^{\alpha\beta}$	Strain rate
c_i	The elastic wave speed
$W_{ij,\beta}$	The kernel gradient with smoothing length h
$\mathrm{d}/\mathrm{d}t$	The time derivative
m	The value of m_s (in the Hoek–Brown criterion)
σ_c	Uniaxial compressive strength
v^{α}	Velocity vector (V)
c_i	The elastic wave speed at the ith particle
$\sigma^{\alpha\beta}$	Cauchy stress tensor (σ)
$\tau^{\alpha\beta}$	Material frame in different objective rate
$\dot{\tau}^{\alpha\beta}$	Stress rate
$\alpha,\ \beta$	Indices for the three spatial directions
a	The half-length of flaw
c	The non-overlapping length

✉ X. P. Zhou
cqxpzhou@hotmail.com

[1] School of Civil Engineering, Chongqing University, 400045 Chongqing, People's Republic of China

[2] School of Resources and Environmental Engineering, Hefei University of Technology, 230009 Hefei, People's Republic of China

[3] Engineering Institute of Engineering Crops, PLA University of Science and Technology, 210007 Nanjing, People's Republic of China

1 Introduction

Rock mass is a heterogeneous geomaterial with various types of pre-existing flaws. The initiation, propagation and coalescence of these pre-existing flaws under loading are significant in the study of rock engineering. The initiation, propagation and coalescence of pre-existing flaws play a decisive role in the mechanical properties of rock mass. Extensive study has been performed on crack propagation for different materials under uniaxial compression in 2D physical experimental works (Bobet and Einstein 1998a, b; Lee and Jeon 2011; Park and Bobet 2009, 2010; Sagong and Bobet 2002; Wong and Einstein 2009a, b; Wong et al. 2001; Zhou et al. 2014) and numerical studies (Zhou et al. 2015a, b; Bobet and Einstein 1998a, b; Liu et al. 2004; Ning et al. 2011a, b; Tang et al. 2001). Although there are many differences in the crack pattern observed by those researchers, there are also common characteristics. Two types of cracks have been regularly observed: primary cracks and secondary cracks. Primary cracks or Wing cracks appear first; they are tensile cracks that start at the tips of the flaw and propagate in a smooth path as the load is increased. Secondary cracks appear later and are responsible, in most cases, for specimen failure; they are described by many authors as shear cracks. Secondary cracks in most cases initiate in a direction coplanar to the pre-existing flaw. In addition, for biaxial loading, the confining pressure can hamper the growth of tensile cracks and thus cause the growth of smaller and more densely distributed pre-existing flaws (Bobet and Einstein 1998a, b; Wang et al. 2014). This can result in localization and shear fractures in the brittle material. The interaction of these localized shear fractures can initiate macro-failure in the rock specimen. Healy et al. (2006a, b) provided a micromechanical model to explain how brittle shear fractures can form obliquely to all three remote principal stresses.

However, it is difficult to conduct experiments to investigate the interactions of 3D pre-existing flaws in samples under uniaxial and biaxial compression. For three-dimensional specimens, tensile cracks or shear cracks occurring in 3D space make the evolution mechanism considerably more complicated and the observation of crack paths substantially more difficult (Yang et al. 2012a, b). Therefore, the similar material polymethly methacrylate (PMMA) is usually employed as the substitute for rock in a 3D pre-existing flaws test. Huang and Wong (2007) performed a series of uniaxial compressive tests on PMMA with pre-existing 3D flaws. Their experimental results showed that the interaction of distinct cracks could either promote or restrain the evolution of cracks in 3D space. However, PMMA could not completely substitute rock in mechanics after all. Moreover, it is difficult to know the stress distribution within a specimen during the loading process, and it is not possible to predict the orientation of it prior to the initiation of cracks. Hence, several important works will be performed on the numerical simulations for the propagation and coalescence of 3D cracks.

The finite element method (FEM) is a very common numerical method used to investigate crack growth and coalescence. Liang et al. (2012) developed and applied the finite element code of rock failure process analysis (RFPA3D) to investigate the initiation and propagation of a 3D surface flaw in rock materials under uniaxial compression. However, when crack propagation and coalescence are involved, remeshing is inevitable, which makes FEM nearly impossible to simulate arbitrary crack growth problems (Bouchard et al. 2000; Liang et al. 2012; Paluszny and Matthai 2009; Wu and Wong 2012).

The extended finite element method (XFEM) (Paluszny and Matthai 2009), the generalized finite element method (GFEM) (Strouboulis et al. 2000a, b) and the particle finite element method (PFEM) (Aubry et al. 2005; Pin et al. 2007) are three very commonly used methods that were developed from the FEM, and PFEM and general particle dynamics (GPD) are meshless methods. By incorporating a proper improvement, all of the above methods can successfully simulate simple and arbitrary crack initiation and growth. However, for some more complicated 3D problems, branch cracking or multi-crack problems that define the enrichment functions can be very difficult.

The numerical manifold method (NMM) (Shi 1991) can be applied to model crack propagation. It is a combination of FEM and the discontinuous deformation analysis (DDA) (Shi and Goodman 1989). NMM has been adopted to solve discontinuous problems involving stationary crack and crack propagation problems (Tsay et al. 1999). However, the crack tips are constrained to stop at the edges of the element, which reduces the accuracy if a crack tip happens to stop inside the element. To improve the accuracy, singular physical covers containing the crack tips are enriched with asymptotic crack-tip functions, and then the stress intensity factors (SIFs) can be accurately evaluated with a regular and relatively coarse mathematical cover system (Zhang et al. 2010).

The boundary element method (BEM) (Chen et al. 1998; Lauterbach and Gross 1998) is another numerical method that is widely applied to model crack propagation. BEM has been recognized as an accurate and efficient numerical technique for solving crack growth problems.

In the method of SPH/SPAM, an interaction between any two particles is only controlled by the kernel function, and the interaction is automatically terminated if one leaves the influence domain of the other. This inherent

fracture mode of processing by defining influence only within the interaction domain of the basis function (Beiseel et al. 2006; Mehra and Chaturvedi 2006) does not to simulate the initiation, propagation and coalescence of flaws well. The material point method (MPM), which is called a particle-in-cell method, is a hybrid arbitrary Lagrangian/Eulerian method suitable for modeling large deformations of history-dependent solids (York et al. 2000; Bardenhagen et al. 2001; Schreyer et al. 2002; Guo and Nairn 2006). MPM saves all discrete continuum field data (displacement, velocity, stress, temperature, etc.) at Lagrangian material points (which are also called particles or markers). While the traditional MPM (Sulsky et al. 1994, 1995), which considers each particle as a concentrated mass, suffers from a 'cell crossing instability' in large deformation problems caused by a jump discontinuity in the gradient of low-order shape functions across cell boundaries.

In addition, the discrete element method (DEM) developed by Cundall and Strack (1979) was applied to simulate the growth of cracks in brittle clay specimens (Vesga et al. 2008). Wang and Mora (2008) used their discrete element model—the lattice solid model to study how cracks propagate when different force–displacement laws are employed. The particle flow code (PFC) is a type of DEM, which is commercially available and is currently applied to solve crack problems (Yoon 2007; Lee and Jeon 2011; Zhang and Wong 2012). The particle flow code in two dimensions (PFC2D) can reproduce the cracks directly by using bond breakage between the circular particles instead of using theories of fracture mechanics, where complex mathematical equations relevant to the stress intensity factor and fracture toughness at the crack tips are implemented (Lee and Jeon 2011; Zhang and Wong 2012).

The object of this study is to propose an efficient and robust numerical method for paths of growth for 3D pre-existing penetration and embedded flaws and fragments in samples under biaxial compression. The novel numerical method is known as general particle dynamics (GPD) (Zhou et al. 2015a, b), which adopts the method of life-death particles, and overcomes the shortcomings of smooth particle hydrodynamics to simulate the local initiation, propagation and coalescence of cracks.

The GPD3D method has several advantages over other traditional continuum methods by simulating the fracturing process and large deformation of materials. For GPD3D, a large deformation and the propagation of cracks in arbitrary and complex paths could also be properly simulated without additional processes due to its adaptation. However, for FEM, it is difficult to model large deformations and the propagation of cracks due to its remeshing feature (Bouchard et al. 2000; Liang et al. 2012; Paluszny and Matthai 2009; Wu and Wong 2012).

GPD3D represents damages directly through the non-linear unified strength criterion (for a 3-D problem) or Hoek–Brown criterion (for a 2-D problem). If particles satisfy the non-linear unified strength criterion or Hoek–Brown criterion, damage occurs. Therefore, the number of discontinuities that can be handled by GPD3D is unlimited. GPD3D easily and accurately models the kinematics of collapsed slopes and simulates failures through intact rock (Zhou et al. 2015a, b). In addition, DEM (Cundall and Strack 1979) has also become a popular method for studying cracking behavior in rocks. By simply breaking the bond when the interaction force between two distinct elements overcomes its tensile or shear strength, DEM can model the fracturing process without assuming where and how the cracks may appear (Wu and Wong 2012). However, relationships between the local and macroscopic constitutive laws are needed in DEM. Establishing these relationships by only using data obtained from classical geomechanical tests is impractical when trying to obtain a desirable single solution set (Donze et al. 2009).

This paper is organized as follows. In Sect. 2, the main steps involved in GPD3D are briefly outlined. The geometries of the numerical model are demonstrated with several examples in Sect. 3. The numerically simulated results are summarized in Sect. 4. Conclusions are then drawn in Sect. 5.

2 Overview of GPD3D

2.1 Governing Equations and Discretization

The conservation equations are expressed in a discretized weak form as (Libersky and Petschek 1991; Libersky et al. 1993; Shaw and Reid 2009)

$$\frac{\mathrm{d}\rho_i}{\mathrm{d}t} = \sum_j m_j v_{ij}^{\beta} W_{ij,\beta} \tag{1}$$

$$\frac{\mathrm{d}v_i^{\alpha}}{\mathrm{d}t} = -\sum_j m_j \left(\frac{\sigma_i^{\alpha\beta}}{\rho_i^2} + \frac{\sigma_j^{\alpha\beta}}{\rho_j^2} + \Pi_{ij} \right) W_{ij,\beta} \tag{2}$$

$$\frac{\mathrm{d}e_i}{\mathrm{d}t} = \frac{1}{2} \sum_j m_j v_{ij}^{\alpha} \left(\frac{\sigma_i^{\alpha\beta}}{\rho_i^2} + \frac{\sigma_j^{\alpha\beta}}{\rho_j^2} + \Pi_{ij} \right) W_{ij,\beta}, \tag{3}$$

where $v_{ij}^{\alpha} = v_i^{\alpha} - v_j^{\alpha}$; $W_{ij,\beta} = \frac{\partial W(x_j - x_i, h)}{\partial x_i^{\beta}}$ is the kernel gradient with smoothing length h; ρ denotes its mass density and e denotes the specific internal energy; x^{α}, v^{α} and $\sigma^{\alpha\beta}$ are the elements for the spatial coordinate (X), velocity vector (V) and Cauchy stress tensor (σ) with tension taken as positive one, $\mathrm{d}/\mathrm{d}t$ is the time derivative taken in the moving Lagrangian framework, and the

superscripts α, $\beta = 1, 2, 3$ are integer indices for the three spatial directions.

If two bodies with significantly different densities come in contact with each other (e.g., rigid mass impacting on soft target), Eqs. (1) through (3) may exhibit a disturbance and subsequent inconsistencies at the interface. This disturbance eventually propagates with time towards the interior from the boundary and affects the final solution(s) (Colagrossi and Landrini 2003). In these cases, a modified form of particle summations is used as (Randles and Libersky 1996; Chen et al. 1999, 2000):

$$\rho_i = \frac{\sum_j m_j W_{ij,\beta}}{\sum_j \left(\frac{m_j}{\rho_j}\right) W_{ij,\beta}}. \tag{4}$$

2.2 The Constitutive Model

Stress components $\sigma^{\alpha\beta} = \tau^{\alpha\beta} - p\delta^{\alpha\beta}$ are computed with pressure p. Pressure p is estimated through the following equation of state as

$$p = k\left(\frac{\rho}{\rho_0} - 1\right), \tag{5}$$

where ρ denotes its real time mass density, ρ_0 is the initial density, and k is the modulus of volume elasticity. The deviatoric stress components $\tau^{\alpha\beta}$ are found through the material frame for a different objective rate as

$$\hat{\dot{\tau}}^{\alpha\beta} = \dot{\tau}^{\alpha\beta} + \tau^{\alpha\gamma}\dot{R}^{\beta\gamma} + \tau^{\gamma\beta}\dot{R}^{\alpha\gamma}, \tag{6}$$

where the strain rate is

$$\dot{\varepsilon}^{\alpha\beta} = \frac{1}{2}\left(\frac{\partial v^{\alpha}}{\partial x^{\beta}} + \frac{\partial v^{\beta}}{\partial x^{\alpha}}\right) \tag{7}$$

and the rotation rate is

$$\dot{R}^{\alpha\beta} = \frac{1}{2}\left(\frac{\partial v^{\alpha}}{\partial x^{\beta}} - \frac{\partial v^{\beta}}{\partial x^{\alpha}}\right), \tag{8}$$

where x^{α} and v^{α} are the elements for the spatial coordinate (X) and velocity vector (V).

This stress rate is related to the traceless strain rate ($\bar{\dot{\varepsilon}}^{\alpha\beta}$) by the shear modulus as

$$\dot{\tau}^{\alpha\beta} = 2G\bar{\dot{\varepsilon}}^{\alpha\beta}, \tag{9}$$

where $\bar{\dot{\varepsilon}}^{\alpha\beta} = \dot{\varepsilon}^{\alpha\beta} - \frac{1}{3}\delta^{\alpha\beta}\dot{\varepsilon}^{\gamma\gamma}$ and G is the shear modulus. Thus, we have

$$\hat{\dot{\tau}}^{\alpha\beta} = 2G\left(\dot{\varepsilon}^{\alpha\beta} - \frac{1}{3}\delta^{\alpha\beta}\dot{\varepsilon}^{\gamma\gamma}\right) + \tau^{\alpha\gamma}\dot{R}^{\beta\gamma} + \tau^{\gamma\beta}\dot{R}^{\alpha\gamma}. \tag{10}$$

2.3 Time-Integration

The above discrete equations are updated in time by a standard two-step predictor–corrector scheme. The time step size is determined based on the Courant–Friedrichs–Levy (CFL) condition as $\Delta t = \min_{i-\text{th particle}}(c_s(h_i/(c_i + |v_i|)))$, with CFL number c_s taken as 0.3 and c_i, v_i as the elastic wave speed and particle velocity at the ith particle, respectively.

2.4 Correction for Consistency

It is obvious from the definition of the immediate neighborhood that the kernel may not always be zero at the cut-off boundary or if the kernel support is not entirely contained within the problem domain. In that case, to preserve the linear consistency with $x_{ij}^{\beta} = x_i^{\beta} - x_j^{\beta}$ and $W_{ij,\beta} = (\partial W(x_i - x_j, h))\big/\partial x_i^{\beta}$, a correction is written as (Chen et al. 1999):

$$\hat{W}_{ij,\beta} = B^{\beta\alpha}W_{ij,\alpha}, \tag{11}$$

where

$$B = A^{-1}, \text{ and } A^{\beta\alpha} = -\sum_j \frac{m_j}{\rho_j} x_{ij}^{\beta} W_{ij,\alpha}. \tag{12}$$

2.5 3D Particle Distribution in the Numerical Models

In GPD3D, it is assumed that the domain consists of particles with the same shape and size and that there is no geometric priority in any orientation (Zhou et al. 2015a, b). The statistical distribution of the elemental mechanical parameters is described by Weibull (1951) distribution function. For the cracking problem, only the uniaxial compressive strength σ_c of particles is described by using Weibull's distribution. The Weibull distribution function is expressed as follows (Weibull 1951):

$$W(x) = \frac{\omega}{x_0}\left(\frac{x}{x_0}\right)^{\omega-1}\exp\left[-\left(\frac{x}{x_0}\right)^{\omega}\right], \tag{13}$$

where ω defines the shape of the Weibull distribution function (it can be referred to as the homogeneity index), x is the mechanical parameter of one particle, and x_0 (the uniaxial compressive strength) is the even value of the parameter for all of the particles. According to the Weibull distribution (Weibull 1951), a larger value of ω indicates that more particles have mechanical properties that have been approximated to the mean value, which describes a more homogeneous rock sample. In present numerical

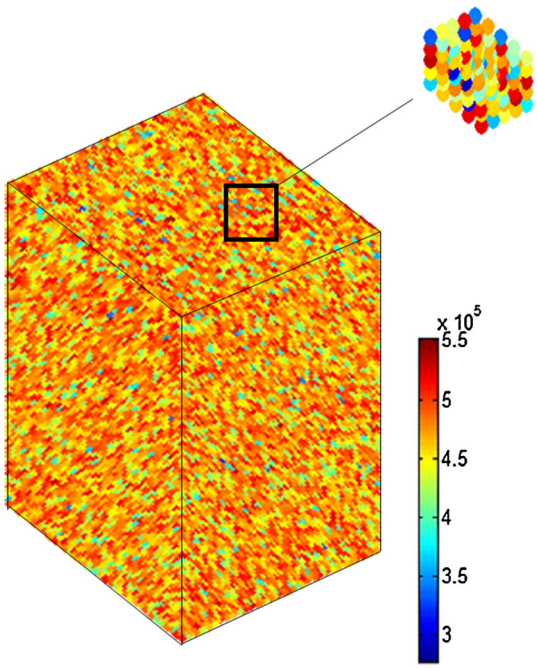

Fig. 1 The uniaxial strength distribution of 3D particles in the numerical model (Pa)

models, the heterogeneity index is $\omega = 20$, as shown in Fig. 1.

2.6 The Damage Model of General Particle Dynamics (GPD3D)

In most cases, rock-like materials fail in a brittle manner. Therefore, the damage initiation and growth in the particles are determined by the damage model of the materials. In this paper, the non-linear unified strength (failure) criterion is applied to determine damage initiation. Damage is initiated from one particle when stresses in the particle satisfy the non-linear unified strength (failure) criterion.

Based on the true triaxial compression test data on rock and considering the effects of intermediate principal stress, the non-linear unified strength (failure) criterion is proposed for rocks as follows (Yu et al. 2002):

$$F = \left[\sigma_1 - \frac{1}{1+b}(b\sigma_2 + \sigma_3)\right]^2 - \frac{m\sigma_c}{1+b} \times (b\sigma_2 + \sigma_3) - s\sigma_c^2 = 0 \quad \text{when} \quad F \geq F' \tag{14}$$

$$F' = \left[\frac{1}{1+b}(b\sigma_2 + \sigma_1) - \sigma_3\right]^2 - m\sigma_c\sigma_3 - s\sigma_c^2 = 0 \quad \text{when} \quad F' \geq F, \tag{15}$$

where σ_c is a uniaxial compressive strength of an intact rock material and b is the intermediate stress parameter. Parameter b is also a parameter for the strength criterion. It is evident that the intermediate principal stress is considered in the non-linear unified strength criterion. The non-linear twin-shear failure criterion can be introduced by the non-linear unified strength criterion when parameter $b = 1$. m and s are the material parameters that are as same as those in the Hoek–Brown criterion, which are defined by Hoek (1983, 1990; Hoek and Brown 1980, 1997) and take the following form:

$$m = m_i \exp\left(\frac{\mathrm{GSI} - 100}{28 - 14D}\right) \tag{16}$$

$$s = \exp\left(\frac{\mathrm{GSI} - 100}{9 - 3D}\right), \tag{17}$$

where D is a disturbance coefficient that varies from 0.0 for the undisturbed in situ rock masses to 1.0 for very disturbed rock masses (Hoek 1983, 1990; Hoek and Brown 1980, 1997) and m_i is the value of m for intact rock and can be obtained from experiments. Parameter m_i varies from four for very fine weak rock such as claystone to 33 for coarse igneous light-colored rock such as granite. In this paper, $m = 10$ and $s = 0.5$.

The non-linear unified strength criterion considers the difference in the tensile and compressive strengths of rocks, the effects of intermediate principal stress on rock strength, the fracturing degree of the rock mass, and the behavior of the failure envelope with a parabola formula. So, the non-linear unified strength criterion has extensive applicability in rock and rock material.

Next, we introduce a parameter f, coined as the 'interaction factor', which defines the level of interaction between the ith and jth particles. This interaction factor f is determined based on the damage in particles. Initially, for undamaged particles, $f = 1$, which implies 'full interaction'. With progressions of damage, f finally becomes zero for a fully damaged particle.

$$D_1 = 0, \text{ and } \quad f = 1, \text{ (if } \sigma_i < \sigma_{\max}) \tag{18}$$

$$D_1 = 1, \text{ and } \quad f = 0, \text{ (if particle damaged)}, \tag{19}$$

where D_1 is the damage factor and f is the interaction factor.

For the method of SPH, an interaction between any two particles is only controlled by the kernel function, and the interaction is automatically terminated if one leaves the influence domain of the other. Therefore, SPH does not simulate the initiation, propagation and coalescence of the flaws well.

In the present numerical method, the non-linear unified strength criterion is applied to determine the damage of particles. The model of influence for damaged particles on neighbors is proposed to determine the level of interaction

between the *i*th and *j*th particles. The statistical distribution of the mechanical parameters of particles is described by the Weibull distribution function, and the effects of the heterogeneity of rock materials are considered. Therefore, the present numerical method is different from the method of SPH. Moreover, GPD can simulate initiation, propagation and coalescence of 3D and 2D pre-existing penetration and embedded flaws.

Therefore, the discrete conservation equations for general particle dynamics (GPD) are expressed as,

$$\frac{\mathrm{d}\rho_i}{\mathrm{d}t} = \sum_{j\in U} m_j v_{ij}^{\beta} W_{ij,\beta} + f \cdot \sum_{j\in D_a} m_j v_{ij}^{\beta} W_{ij,\beta} \tag{20}$$

$$\frac{\mathrm{d}v_i^{\alpha}}{\mathrm{d}t} = -\sum_{j\in U} m_j \left(\frac{\sigma_i^{\alpha\beta}}{\rho_i^2} + \frac{\sigma_j^{\alpha\beta}}{\rho_j^2} + \Pi_{ij}\right) W_{ij,\beta} - f \cdot \sum_{j\in D_a} m_j \left(\frac{\sigma_i^{\alpha\beta}}{\rho_i^2} + \frac{\sigma_j^{\alpha\beta}}{\rho_j^2} + \Pi_{ij}\right) W_{ij,\beta} \tag{21}$$

$$\frac{\mathrm{d}e_i}{\mathrm{d}t} = \frac{1}{2}\sum_{j\in U} m_j v_{ij}^{\alpha} \left(\frac{\sigma_i^{\alpha\beta}}{\rho_i^2} + \frac{\sigma_j^{\alpha\beta}}{\rho_j^2} + \Pi_{ij}\right) W_{ij,\beta} + \frac{f}{2} \cdot \sum_{j\in D_a} m_j v_{ij}^{\alpha} \left(\frac{\sigma_i^{\alpha\beta}}{\rho_i^2} + \frac{\sigma_j^{\alpha\beta}}{\rho_j^2} + \Pi_{ij}\right) W_{ij,\beta}, \tag{22}$$

where U denotes undamaged particles and D_a denotes damaged particles.

Once damage is initiated from one particle, their interactions will no longer be the same as in the undamaged material. Although the damaged particles do not disappear and are still in the influence domain of others, the damaged particle is traction free and the damaged particle has no influence on the surrounding particles in the stress calculation because the interaction factor f is zero, as shown in Eqs. (5) through (9). For the damaged particles, because its stresses become zero, the surrounding living particles have no influence on them. A new boundary is formed as shown in Fig. 2.

3 The Numerical Results are Compared with the Experimental Results

3.1 The Coalescence Patterns of the Two Pre-existing Penetrating Flaws in the Sample Under Compression

To validate GPD3D, the numerical results obtained from GPD3D will be compared with the experimental results of Bobet and Einstein (1998a, b) that were obtained from the prismatic blocks described in Fig. 4. One sample with two pre-existing penetrating flaws under compression is depicted in Fig. 3.

The dimensions and strength of the numerical sample are consistent with those of the experimental specimen used in tests (Bobet and Einstein 1998a, b). The $49 \times 100 \times 20 = 98{,}000$ particles represent a sample geometry of 76.2 (width) × 152.4 (length) × 30 (thickness) mm in scale, as shown in Fig. 3a. Two pre-existing penetrating flaws have a length of 12.7 mm (0.5 in.) and an aperture of 0.10 mm (0.004 inch), as shown in Fig. 3b. The flaw geometry is defined by three parameters: flaw inclination angle $\beta = 45°$, spacing (s_0), and continuity (c) (see Fig. 3b).

Under compression, the sample containing the two pre-existing penetrating flaws is tested with lateral stresses of 0,

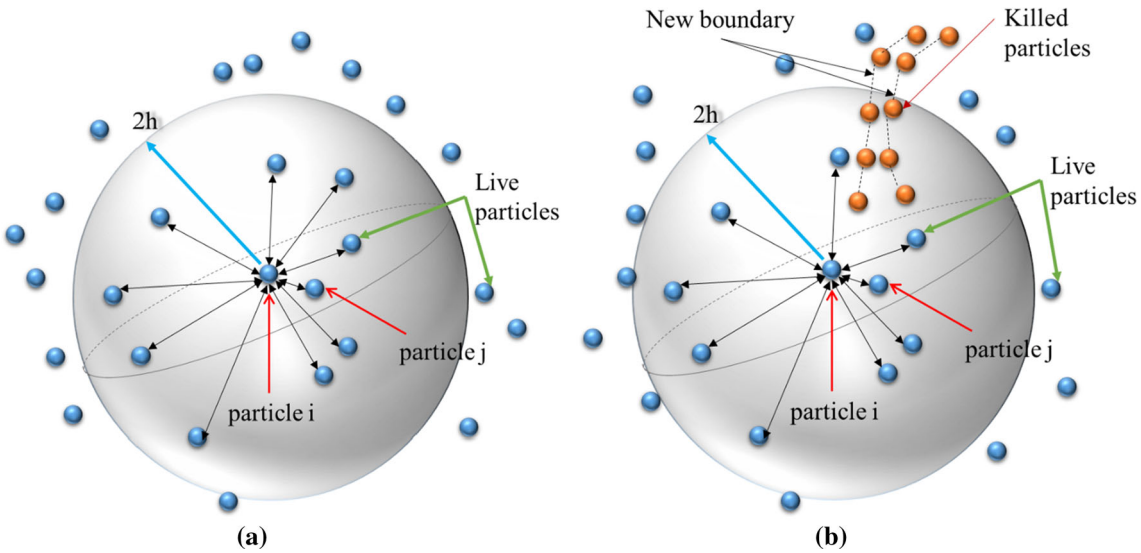

Fig. 2 3D particle discretization: **a** undamaged configuration, **b** cracked configuration

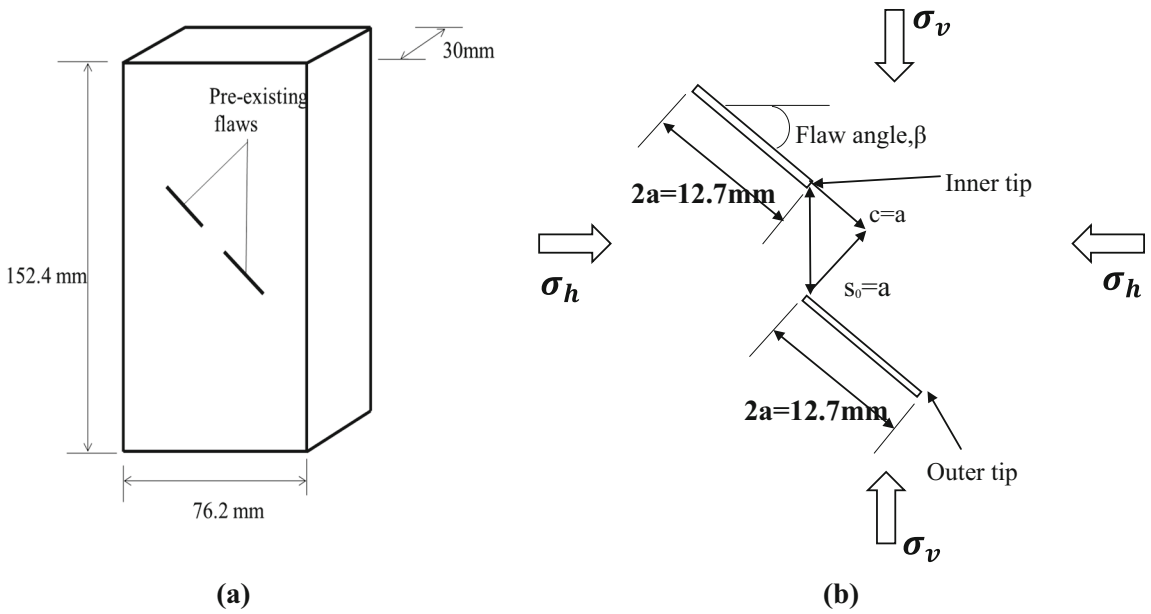

Fig. 3 Geometries of rock specimens containing the two pre-existing penetrating flaws. **a** Overall view. **b** Detail (Bobet and Einstein 1998a, b)

2.5 and 5 MPa. The parameters of the material properties are listed as follows (Bobet and Einstein 1998a, b): the average uniaxial compressive strength (σ_c) is 34.5 MPa, the average Young's Modulus is 5960 MPa, and the average Poisson's ratio is 0.15.

Figure 4a–f shows the coalescence patterns of two pre-existing penetrating flaws in the numerical samples under compression with a lateral stress of 0, 2.5 and 5 MPa, respectively.

When the sample containing two pre-existing collinear flaws is subjected to uniaxial compression, the wing cracks are first initiated from the inner and outer tips of the pre-existing flaws, and wing cracks propagate along the direction of the maximum principal stress. Then, the quasi-coplanar secondary cracks are initiated from the inner tips of the pre-existing flaws. Next, the coalescence of the quasi-coplanar secondary cracks occurs. Finally, the splitting failure for the sample occurs. The types of coalescing fracture are the coalescence of the quasi-coplanar secondary cracks. The failure pattern of the sample containing two pre-existing collinear penetrating flaws subjected to uniaxial compression is controlled by splitting failure, as shown in Fig. 4a. The numerical results are in good agreement with the experimental results (Bobet and Einstein 1998a, b).

When the sample containing two pre-existing collinear flaws is subjected to biaxial compression with a lateral stress of 2.5 MPa, the quasi-coplanar secondary cracks are first initiated from the inner and outer tips of the pre-existing flaws. Then, wing cracks are initiated from the inner and outer tips of the pre-existing flaws. Next, the coalescence of the quasi-coplanar secondary cracks occurs. Finally, shear failure of the sample occurs. However, the lengths of the wing cracks in the sample subjected to biaxial compression are considerably less than that in the sample subjected to uniaxial compression. The types of coalescing fracture are the coalescence of the quasi-coplanar secondary cracks. The failure pattern of the sample subjected to biaxial compression with a lateral stress of 2.5 MPa is controlled by shear failure, as shown in Fig. 4c.

When the sample containing two pre-existing non-collinear flaws is subjected to biaxial compression with a lateral stress of 5 MPa, the secondary cracks are first initiated from the inner and outer tips of the pre-existing flaws. Then, the coalescence of the quasi-coplanar secondary cracks and tensile cracks occurs. Next, the wing cracks are initiated from the center of the pre-existing flaws. Finally, shear failure of the sample occurs. The types of coalescing fracture are the coalescence of the quasi-coplanar secondary cracks and tensile cracks. The failure pattern of the sample containing two pre-existing non-collinear penetrating flaws subjected to biaxial compression with a lateral stress of 5 MPa is controlled by shear failure, as shown in Fig. 4e.

The coalescence pattern and failure mode of the numerical sample is nearly the same as the experimental one (Bobet and Einstein 1998a, b), as shown in Fig. 4b, d and f.

As shown in Fig. 5, the initiation stress of a quasi-coplanar secondary crack and a wing crack, and the coalescence stress and the failure stress increase when increasing the lateral stress. When the sample is subjected

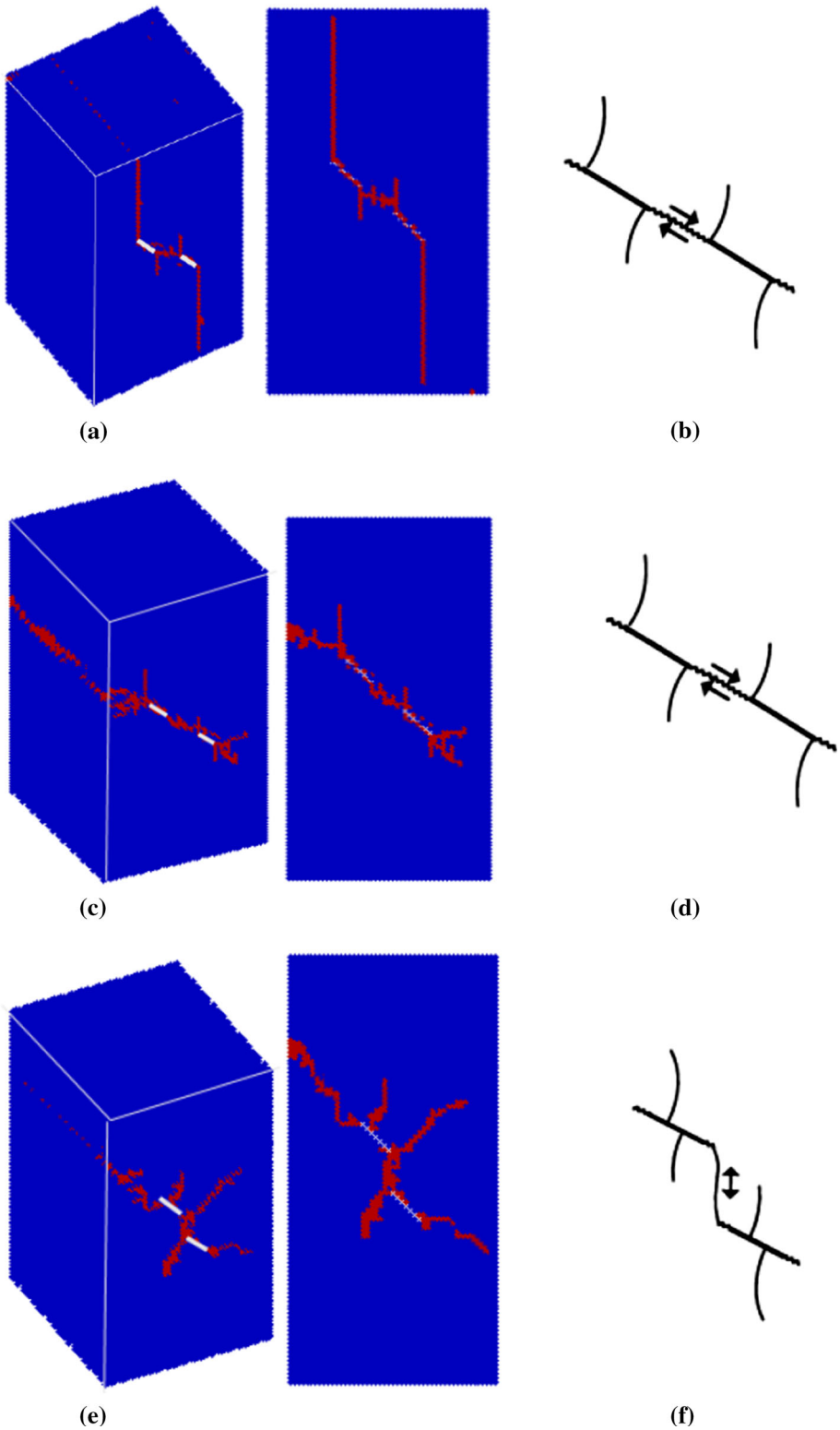

Fig. 4 Coalescence patterns of two pre-existing penetrating flaws in the samples under uniaxial and biaxial compression: **a** numerical result in the sample with spacing $s_0 = 0$, continuity $c = 2a$ and lateral stress of 0 MPa; **b** experimental result in the sample with spacing $s_0 = 0$, continuity $c = 2a$ and lateral stress of 0 MPa; **c** numerical result in the sample with spacing $s_0 = 0$, continuity $c = 2a$ and lateral stress of 2.5 MPa; **d** experimental result in the sample with spacing $s_0 = a$, continuity $c = a$ and lateral stress of 2.5 MPa; **e** numerical result in the sample with spacing $s_0 = a$, continuity $c = a$ and lateral stress of 5 MPa; **f** experimental result in the sample with spacing $s_0 = a$, continuity $c = a$ and lateral stress of 5 MPa

to uniaxial compression, the wing cracks are initiated earlier than the secondary cracks. When the lateral stress is greater than 2.5 MPa, the wing cracks are initiated later than the secondary cracks. The numerical results in Fig. 5a are in good agreement with the experimental results in Fig. 5b (Bobet and Einstein 1998a, b).

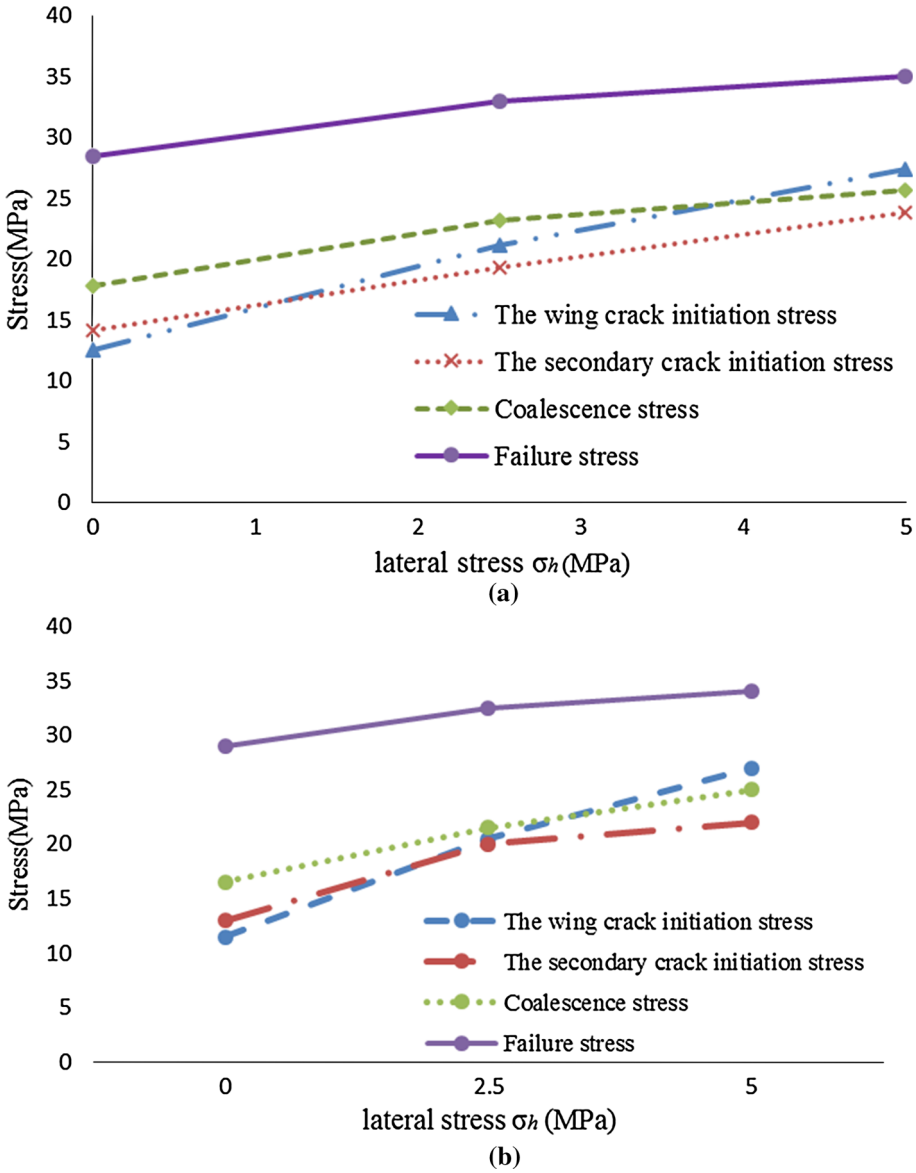

Fig. 5 Results of samples under uniaxial compression and biaxial compression with different lateral stresses: **a** numerical results; **b** experimental results

3.2 The Coalescence Patterns of Three Pre-existing Penetrating Flaws in the Sample Under Uniaxial Compression

Yang et al. (2012b) analyzed the fracture coalescence behavior of brittle sandstone. Rectangular prismatic sandstone specimens (80 × 160 × 30 mm in size) containing three fissures were tested under uniaxial compression. The same parameters are used in the simulation process in this paper to validate the accuracy of GPD3D. The coalescence patterns are plotted in Fig. 6.

As shown in Fig. 6, the types of crack coalescence for the numerical sample and the experimental specimen for brittle sandstone with three pre-existing penetrating flaws are nearly the same. All of the crack coalescences can be simply classified into two types, which are tensile coalescence (T mode) and compression coalescence (C mode). It is found from Fig. 6 that GPD3D can simulate the failure process of the brittle materials well.

4 The Numerical Results and Discussions

4.1 Geometries of the Numerical Models

Figure 7 shows the setup of the numerical model containing the four pre-existing flaws. In the numerical model, the size of the sample is 90 (width) × 150 (length) × 70 (thickness) mm, and the alignment of the 3D macroscopic pre-existing penetrating flaws is depicted in Fig. 7

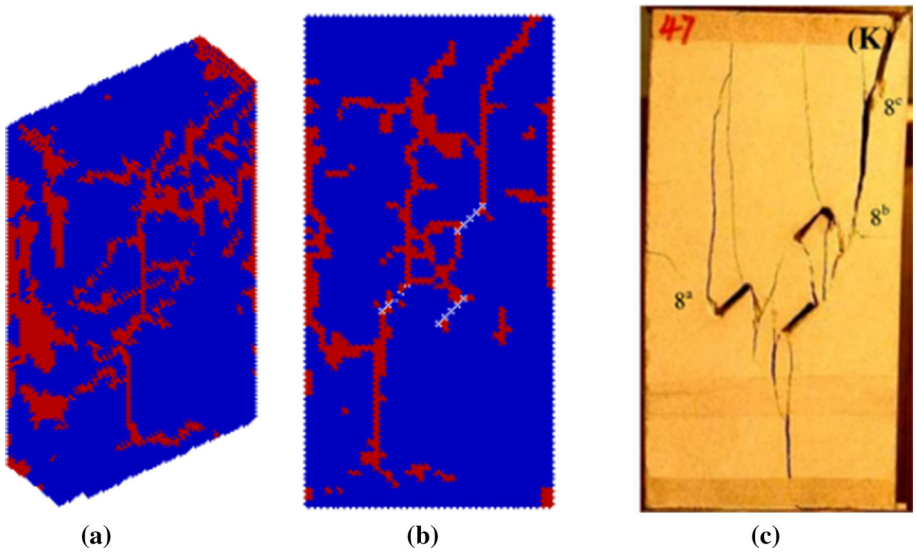

Fig. 6 Paths of crack propagation in the sample containing three pre-existing penetrating flaws: **a** 3D drawing of crack propagation paths, **b** the cross section of crack propagation paths, **c** crack coalescence process of a sandstone specimen containing three flaws under uniaxial compression (Yang et al. 2012b)

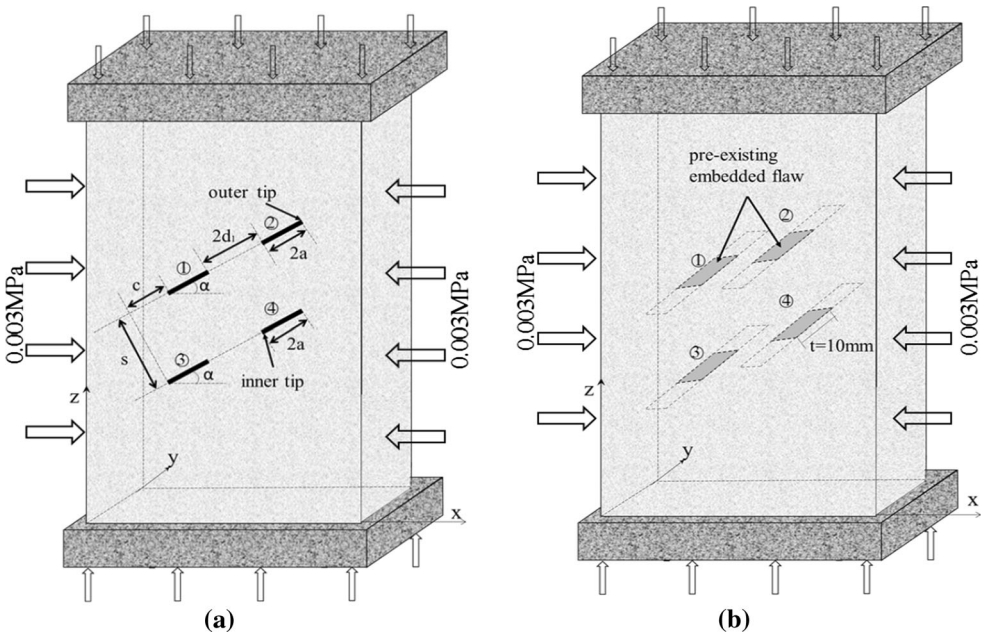

Fig. 7 The layout of samples containing four pre-existing flaws under biaxial compression: **a** the pre-existing penetrating flaws, **b** the pre-existing embedded flaws

Six cases are considered in total. The samples contain the four pre-existing flaws. The samples containing four pre-existing penetrating flaws under biaxial compression are depicted in Fig. 7a, and the samples containing four pre-existing embedded flaws with width $t = 10$ mm, which are located in the middle of the sample along the y direction, are plotted in Fig. 7b. For convenience of description and discussion, the pre-existing flaws are marked with ①, ②, ③ and ④, as shown in Fig. 7. We refer to the pre-existing fracture as a flaw and the initiated and propagated fracture as a crack. The flaw length $2a$ is 10 mm, and the bridge length between the tips of the flaws $2d_1$ is 20 mm. The perpendicular distance between the two adjacent rows is fixed at $s_0 = 20$ mm. One group of samples (from case 1 to case 3) contains four pre-existing penetrating flaws with different non-overlapping lengths ($c = 0$,10 and 20 mm), and the other group of samples (from case 4 to case 6) contains four pre-existing embedded flaws with different non-overlapping lengths ($c = 0$, 10 and 20 mm). The lateral stress is 0.003 MPa in the two groups.

In the simulation, $45 \times 75 \times 35 = 118{,}125$ particles represent a sample geometry of 90 (width) $\times$ 150 (length) $\times$ 70 (thickness) mm in scale.

Figure 1 shows the 3D hexahedral particle distribution in the numerical model. The uniaxial compression strength of each hexahedral particle is assumed to follow the

Weibull distribution. A displacement control of 0.002 m per second was applied axially on the top and bottom of all specimens.

4.2 Numerical Results for Rock Specimens of Group 1

Cases 1, 2 and 3 represent the samples containing pre-existing penetrating flaws with a non-overlapping length of $c = 0$, $c = 10$ and $c = 20$ mm, respectively. Figure 8 shows the numerical results of the numerical models containing four pre-existing penetrating flaws with different non-overlapping lengths under uniaxial compression. The numerical results for the samples containing four pre-existing penetrating flaws with different non-overlapping lengths under biaxial compression are plotted in Fig. 9.

The differences between the samples containing the four pre-existing penetrating flaws with non-overlapping length $c = 0$ mm under uniaxial compression in Fig. 8a and under biaxial compression in Fig. 9a are that: (1) the length of the wing cracks initiating from the outer tips of flaw ② and flaw ③ under uniaxial compression is longer than that under biaxial compression (the main reason is that the lateral stress hampers the growth of the wing cracks); (2) the coalescence types of the four pre-existing penetrating flaws in the sample under biaxial compression are different from those in the sample under uniaxial compression; the coalescence of oblique secondary cracks and the coalescence of the quasi-coplanar secondary cracks are observed in the sample under biaxial compression, while the coalescence of the out-of-plane shear crack and the wing crack are found in the sample under uniaxial compression; and (3) the failure pattern of the rock-like sample subjected to uniaxial compression is a splitting failure, while the failure pattern of the sample subjected to biaxial compression is a shear failure.

The differences between the samples containing four pre-existing penetrating flaws with non-overlapping length $c = 10$ mm under uniaxial compression in Fig. 8b and under biaxial compression in Fig. 9b are that: (1) there is

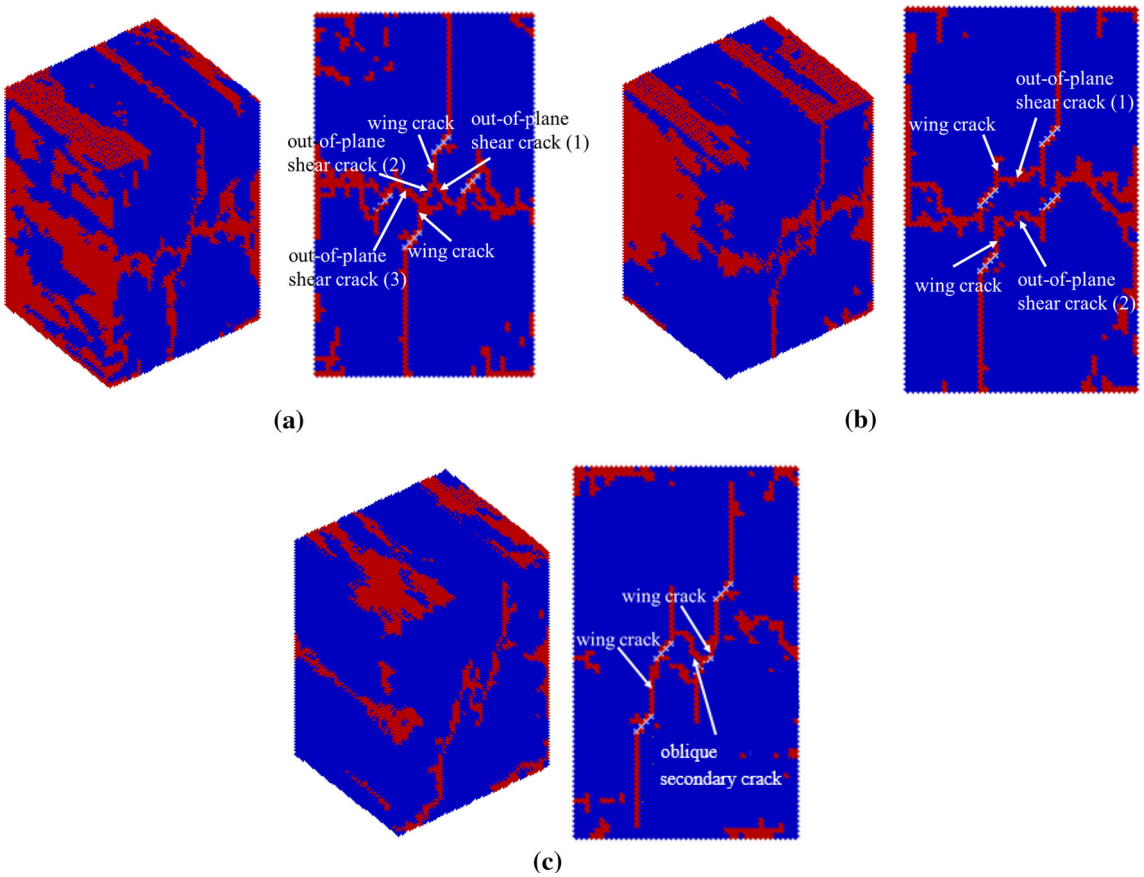

Fig. 8 Paths of crack propagation in samples containing the four pre-existing penetrating flaws under uniaxial compression: **a** 3D drawing of propagation paths of the pre-existing flaws and the cross section of propagation paths of the pre-existing flaws with non-overlapping length $c = 0$ mm in the sample; **b** 3D drawing of propagation paths of the pre-existing flaws and the cross section of propagation paths of the pre-existing flaws with non-overlapping length $c = 10$ mm in the sample; **c** 3D drawing of propagation paths and the cross section of propagation paths of the pre-existing flaws with non-overlapping length $c = 20$ mm in the sample

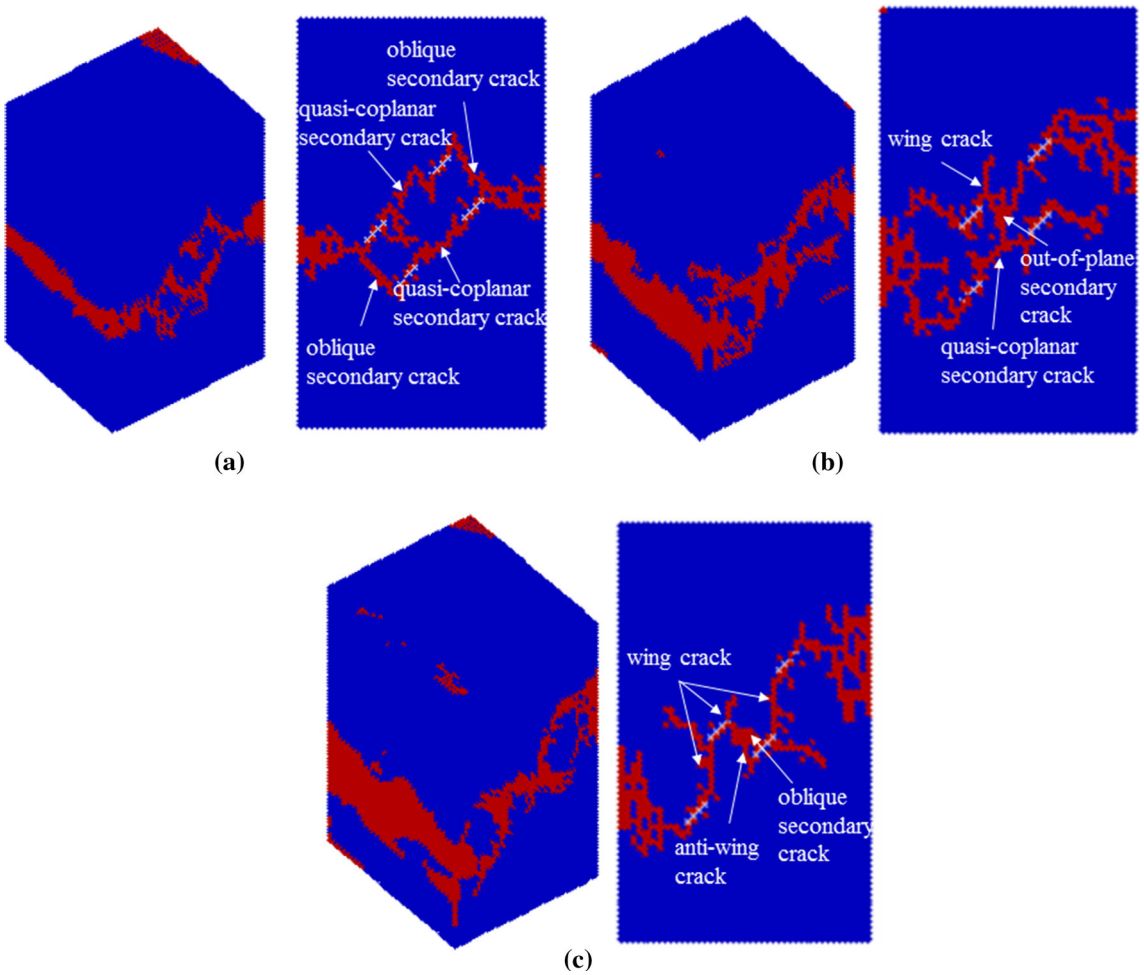

Fig. 9 Paths of crack propagation in samples containing the four pre-existing penetrating flaws under biaxial compression with the lateral stress of 0.003 MPa: **a** 3D drawing of propagation paths of the pre-existing flaws and the cross section of propagation paths of the pre-existing flaws with non-overlapping length $c = 0$ mm in the sample; **b** 3D drawing of propagation paths of the pre-existing flaws and the cross section of propagation paths of the pre-existing flaws with non-overlapping length $c = 10$ mm in the sample; **c** 3D drawing of propagation paths and the cross section of propagation paths of the pre-existing flaws with non-overlapping length $c = 20$ mm in the sample

no wing crack initiating from the outer tips of flaw ② and flaw ③ in the sample subjected to biaxial compression, while wing cracks initiating from the outer tips of flaw ② and flaw ③ propagate to the top and bottom boundaries in the sample subjected to uniaxial compression; (2) coalescence types of the four pre-existing penetrating flaws in the sample under biaxial compression are different from those in the sample under uniaxial compression; the coalescence of the out-of-plane secondary crack and the wing crack is observed in the sample under uniaxial compression, whereas the coalescence of the quasi-coplanar secondary cracks, the coalescence of the wing crack and the out-of-plane secondary crack and the quasi-coplanar secondary crack are observed in the sample under biaxial compression; and (3) the failure pattern of the sample subjected to uniaxial compression is a splitting failure, while the failure pattern of the sample subjected to biaxial compression is a shear failure.

The differences between the samples containing four pre-existing penetrating flaws with non-overlapping length $c = 20$ mm under uniaxial compression in Fig. 8c and under biaxial compression in Fig. 9c are that: (1) the growth length of the wing cracks in the sample subjected to uniaxial compression is longer than that of the wing cracks in the sample subjected to biaxial compression; (2) the wing cracks in the sample under uniaxial compression are smooth, while bifurcation exists in the wing cracks in the sample under biaxial compression; (3) coalescence types of four pre-existing penetrating flaws in the sample under uniaxial compression are different from those in the sample under biaxial compression and the coalescence of the wing cracks and the coalescence of the oblique secondary crack

and the wing crack are observed in the sample under uniaxial compression, while the coalescence of the wing cracks, the coalescence of the oblique secondary cracks, and the coalescence of the oblique secondary crack and the anti-wing crack are observed in the sample under biaxial compression; and (4) the failure pattern of the sample subjected to uniaxial compression is a splitting failure, while the failure pattern of the sample subjected to biaxial compression is a shear failure.

With increasing biaxial loads, the secondary cracks keep growing in the samples. These shear fractures propagate towards the left and right sides of the samples, while there are nearly no wing cracks initiating from the tips of the pre-existing flaws in samples under biaxial compressive loads. The samples that contain four pre-existing penetrating flaws under uniaxial compression are split into fragments in a tensile rip failure mode, as shown in Fig. 8. However, samples that contain the four pre-existing penetrating flaws under biaxial compression are split into fragments in a shear failure mode as depicted in Fig. 9, and macro-shear fractures are also observed on the left and right side of these samples subjected to biaxial compression due to the propagation and coalescence of the secondary cracks.

4.3 Numerical Results for Rock Specimens of Group 2

Cases 4, 5 and 6 represent the samples containing four pre-existing embedded flaws with non-overlapping lengths of $c = 0$, $c = 10$ and $c = 20$ mm, respectively. Figure 10 shows the numerical results for samples containing the four pre-existing embedded flaws with different non-overlapping lengths under uniaxial compression. The numerical results of the samples containing four pre-existing embedded flaws with different non-overlapping lengths under biaxial compression are plotted in Fig. 11.

The differences between the samples containing the four pre-existing embedded flaws with non-overlapping length $c = 0$ mm under uniaxial compression in Fig. 10a and under biaxial compression in Fig. 11a are that: (1) there is no wing crack initiating from the outer tips of flaw ② and flaw ③ in the sample subjected to biaxial compression, while wing cracks initiated from the outer tips of flaw ② and flaw ③ propagate along the direction of the maximum principal stress in the sample subjected to uniaxial compression; (2) coalescence types of the four pre-existing embedded flaws in the sample under biaxial compression are different from those in the sample under uniaxial compression; the coalescence of the out-of-plane secondary crack and the quasi-coplanar secondary crack and the coalescence of the quasi-coplanar secondary cracks are observed in the sample under uniaxial compression, while the coalescence of the quasi-coplanar secondary cracks and the coalescence of the oblique secondary cracks are found in the sample under biaxial compression; and (3) the failure pattern of the sample subjected to uniaxial compression is mainly controlled by a splitting failure, while the failure pattern of the sample subjected to biaxial compression is mainly controlled by a shear failure.

The differences between the samples containing four pre-existing embedded flaws with non-overlapping length $c = 10$ mm under uniaxial compression in Fig. 10b and under biaxial compression in Fig. 11b are that: (1) there is no wing crack initiated from the outer tips of flaw ② and flaw ③ in the sample under biaxial compression, while wing cracks initiated from the outer tips of flaw ② and flaw ③ propagate along the direction of the maximum principal stress in the sample subjected to uniaxial compression; (2) coalescence types of four pre-existing embedded flaws in the sample under biaxial compression are different from those in the sample under uniaxial compression; the coalescence of quasi-coplanar secondary cracks and the coalescence of the oblique secondary cracks are observed in the sample under uniaxial compression, while the coalescence of the anti-wing crack, out-of- plane secondary crack and the oblique secondary crack, the coalescence of quasi-coplanar secondary cracks, and the coalescence of the oblique secondary cracks are observed in the sample under biaxial compression; and (3) the failure pattern of the sample subjected to uniaxial compression is mainly controlled by a splitting failure, while the failure pattern of the sample under biaxial compression is mainly controlled by a shear failure.

The differences between the samples containing four pre-existing embedded flaws with non-overlapping length $c = 20$ mm under uniaxial compression in Fig. 10c and under biaxial compression in Fig. 11c are that: (1) the length of the wing cracks initiating from the outer tips of flaw ② and flaw ③ under uniaxial compression is longer than that under biaxial compression (the main reason is that the lateral stress hampers the growth of wing cracks); (2) coalescence types of four pre-existing embedded flaws in the sample under biaxial compression are different from those in the sample under uniaxial compression; the coalescence of the oblique secondary cracks are observed in the sample under uniaxial compression, while the coalescence of the quasi-coplanar secondary cracks, the coalescence of the oblique secondary cracks, and the coalescence of the oblique secondary crack and the wing crack are found in the sample subjected to biaxial compression; and (3) the failure pattern of the sample subjected to uniaxial compression are mainly controlled by a splitting failure, while the failure pattern of the sample subjected to biaxial compression is mainly controlled by a shear failure.

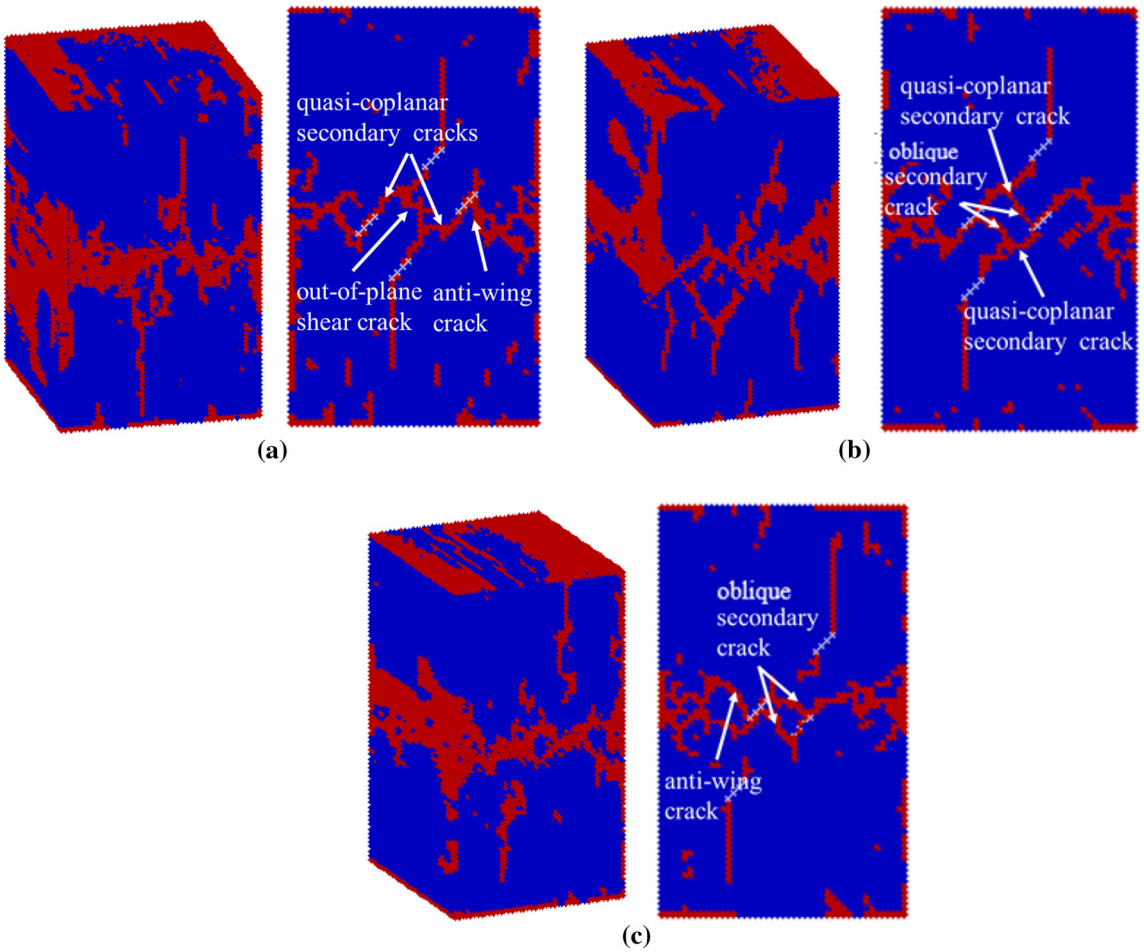

Fig. 10 Paths of crack propagation in samples containing the four pre-existing embedded flaws under uniaxial compression: **a** 3D drawing of propagation paths of the pre-existing flaws and the cross section of propagation paths of the pre-existing flaws with non-overlapping length $c = 0$ mm in the sample; **b** 3D drawing of propagation paths of the pre-existing flaws and the cross section of propagation paths of the pre-existing flaws with non-overlapping length $c = 10$ mm in the sample; **c** 3D drawing of propagation paths and the cross section of propagation paths of the pre-existing flaws with non-overlapping length $c = 20$ mm in the sample

5 Conclusions and Discussions

GPD3D is introduced to investigate the fracture propagation and coalescence of rock-like materials with macroscopic pre-existing flaws under biaxial compressive loads. The main feature of GPD3D is that it can simulate the evolution of internal cracks in three-dimensional space, which is considerably more complex than the two-dimensional crack regimes that are commonly studied. The present numerical simulation focuses on the non-overlapping length and the types of pre-existing flaws in the rock-like samples under biaxial compression. Although the role of these parameters needs additional experimental and theoretical analysis and the propagation and coalescence processes of 3D cracks under complex loading styles should be further investigated, the present numerical results demonstrate many phenomena that have already been observed in laboratory experiments. However, many of these fracture phenomena direct us to the necessity of additional experiments. This present study highlights some interesting phenomena for improving the understanding of the mechanism of 3D rock fracturing. Some of the main conclusions are summarized as follows:

The propagation and coalescence processes of the wing cracks, the oblique secondary cracks, the out-of-plane shear cracks, the anti-wing cracks and the quasi-coplanar shear crack in numerical samples subjected to biaxial compression can be numerically simulated by GPD3D. Although the coalescence of cracks between macroscopic pre-existing flaws cannot be easily observed in laboratory testing, they can be predicted by numerical modeling.

With increasing lateral stress, the secondary cracks keep growing in the samples, while the growth of the wing cracks is restrained. The main reason is that lateral stress

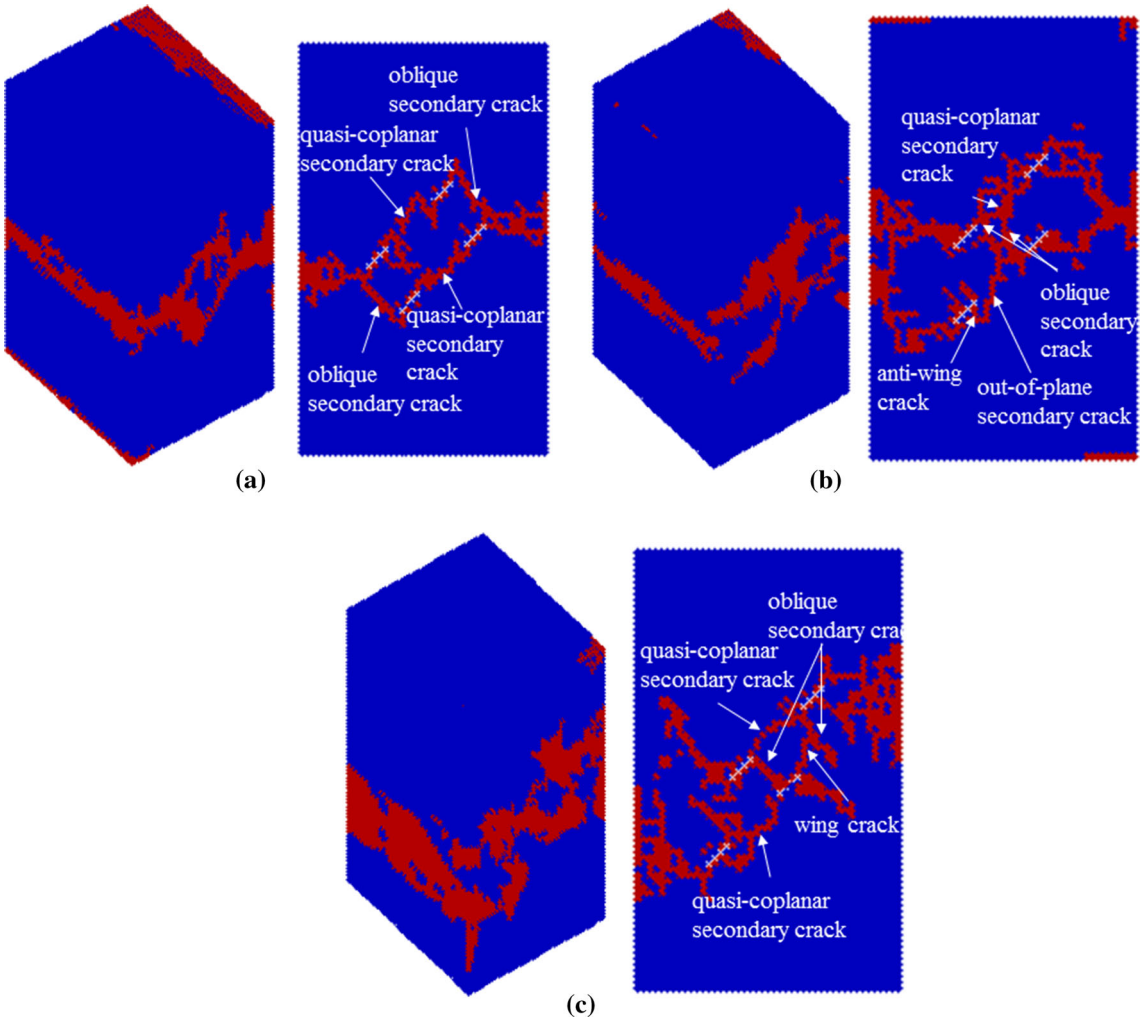

Fig. 11 Paths of crack propagation in samples containing four pre-existing embedded flaws under biaxial compression with the lateral stress of 0.003 MPa: **a** 3D drawing of propagation paths of the pre-existing flaws and the cross section of propagation paths of the pre-existing flaws with non-overlapping length $c = 0$ mm in the sample; **b** 3D drawing of propagation paths of the pre-existing flaws and the cross section of propagation paths of the pre-existing flaws with non-overlapping length $c = 10$ mm in the sample; **c** 3D drawing of propagation paths and the cross section of propagation paths of the pre-existing flaws with non-overlapping length $c = 20$ mm in the sample

hampers the growth of wing cracks. The samples subjected to biaxial compression are mainly split into fragments in a shear failure mode, which is different from a splitting failure of the samples subjected to uniaxial compression.

For specimens with macroscopic pre-existing flaws, the simulated types of cracks, the simulated failure modes and the simulated coalescence types are in good agreement with the experimental results. It is found from the numerical results that GPD3D can simulate the failure process of the brittle materials well.

Acknowledgments This work was supported by project 973 (Grant No. 2014CB046903), the National Natural Science Foundation of China (Nos. 51325903 and 51279218), and the Natural Science Foundation Project of CQ CSTC (Nos. CSTC, cstc2013kjrcljrccj0001 and cstc2013jcyjys30002).

References

Aubry R, Idelsohn SR, Oñate E (2005) Particle finite element method in fluid mechanics including thermal convection–diffusion. Comput Struct 83:1459–1475

Bardenhagen S, Guilkey J, Roessig K, Brackbill J, Witzel W, Foster J (2001) An improved contact algorithm for the material point method and application to stress propagation in granular material. Comp Model Eng 2:509–522

Beiseel SR, Gerlach CA, Johnson GR (2006) Hypervelocity impact computations with finite elements and meshfree particles. Int J Impact Eng 33:80–90

Bobet A, Einstein HH (1998a) Fracture coalescence in rock-type materials under uniaxial and biaxial compression. Int J Rock Mech Min Sci 35:863–888

Bobet A, Einstein HH (1998b) Numerical modeling of fracture coalescence in a model rock material. Int J Fract 92:221–252

Bouchard PO, Baya F, Chastela Y, Tovena I (2000) Crack propagation modelling using an advanced remeshing technique. Comput Methods Appl Mech Eng 189:723–742

Chen JK, Beraun JE, Carney TC (1999) A corrective smoothed particle method for boundary value problems in heat conduction. Int J Numer Methods Eng 46:231–252

Chen CS, Pan E, Amadei B (1998) Fracture mechanics analysis of cracked discs of anisotropic rock using the boundary element method. Int J Rock Mech Min 35:195–218

Chen JS, Yoon S, Wang HP, Liu WK (2000) An improved reproducing kernle particle method for nearly incompressibles hyperelastic solids. Comput Methods Appl Mech Eng 181:117–145

Colagrossi A, Landrini M (2003) Numerical simulation of interfacial flows by smoothed particle hydrodynamics. J Comput Phys 191:448–475

Cundall PA, Strack ODL (1979) A discrete numerical model for granular assemblies. Geotechnique 29:47–65

Donze FV, Richefeu V, Magnier SA (2009) Advances in discrete element method applied to soil rock and concrete mechanics. Electron J Geotech Eng 8:1–44

Guo Y, Nairn J (2006) Three-dimensional dynamic fracture analysis using the material point method. Comp Model Eng 16:141–155

Healy D, Jones RR, Holdsworth RE (2006a) New insights into the development of brittle shear fractures from a 3-D numerical model of microcrack interaction. Earth Planet Sci Lett 249:14–28

Healy D, Jones RR, Holdsworth RE (2006b) Three-dimensional brittle shear fracturing by tensile crack interaction. Nature 439:64–67

Hoek E (1983) Strength of jointed rock masses. Geotechnique 33:187–223

Hoek E (1990) Estimating Mohr-Coulomb friction and cohesion values from the Hoek–Brown failure criterion. Int J Rock Mech Min 27:227–229

Hoek E, Brown ET (1980) Empirical strength criterion for rock masses. J Geotech Geoenviron 106(GT9):1013–1036

Hoek E, Brown ET (1997) Practical estimate the rock mass strength. Int J Rock Mech Min 34:1165–1186

Huang ML, Wong RHC (2007) Experimental study on propagation and coalescence mechanisms of 3D surface cracks. Chin J Rock Mech Eng 26:1794–1799

Lauterbach B, Gross D (1998) Crack growth in brittle solids under compression. Mech Mater 29:81–92

Lee H, Jeon S (2011) An experimental and numerical study of fracture coalescence in pre-cracked specimens under uniaxial compression. Int J Solids Struct 48:979–999

Liang ZZ, Xing H, Wang SY, Williams DJ, Tang CA (2012) A three-dimensional numerical investigation of the fracture of rock specimens containing a pre-existing surface flaw. Comput Geotech 45:19–33

Libersky LD, Petschek AG (1991) Smoothed particle hydrodynamics with strength of materials. In: Trease H, Friits J, Crowley W (eds) Proceedings of the Next Free Lagrange Conference, vol 395. Springer, New York, pp 248–257

Libersky LD, Petschek AG, Carney TC, Hipp JR, Allahdadi FA (1993) High strain Lagrangian hydrodynamics: a three dimensional SPH code for dynamic material response. J Comput Phys 109:67–75

Liu HY, Kou SQ, Lindqvist PAPA, Tang CA (2004) Numerical simulation of shear fracture (mode II) in heterogeneous brittle rock. Int J Rock Mech Min 41:14–19

Mehra V, Chaturvedi S (2006) High velocity impact of metal sphere on thin metallic plates: a comparative smooth particle hydrodynamics study. J Comput Phys 212:318–337

Ning YJ, An XM, Ma GW (2011a) Footwall slope stability analysis with the numerical manifold method. Int J Rock Mech Min 48:964–975

Ning Y, Yang J, An X, Ma G (2011b) Modelling rock fracturing and blast-induced rock mass failure via advanced discretisation within the discontinuous deformation analysis framework. Comput Geotech 38:40–49

Paluszny A, Matthai SK (2009) Numerical modeling of discrete multi-crack growth applied to pattern formation in geological brittle media. Int J Solids Struct 46:3383–3397

Park CH, Bobet A (2009) Crack coalescence in specimens with open and closed flaws: a comparison. Int J Rock Mech Min 46:819–829

Park CH, Bobet A (2010) Crack initiation, propagation and coalescence from frictional flaws in uniaxial compression. Eng Fract Mech 77:2727–2748

Pin FD, Idelsohn SR, Oñate E, Aubry R (2007) The ALE/Lagrangian particle finite element method: a new approach to computation of free-surface flows and fluid–object interactions. Comput Fluids 36:27–38

Randles PW, Libersky LD (1996) Smoothed particle hydrodynamics some recent improvements and applications. Comput Methods Appl Mech Eng 138:375–408

Sagong M, Bobet A (2002) Coalescence of multiple flaws in a rock-model material in uniaxial compression. Int J Rock Mech Min 39:229–241

Schreyer H, Sulsky D, Zhou S (2002) Modeling delamination as a strong discontinuity with the material point method. Comput Methods Appl Mech Eng 191:2483–2507

Shaw A, Reid SR (2009) Applications of SPH with the acceleration correction algorithm in structural impact computations. Curr Sci 97(8):1177–1186

Shi GH (1991) Manifold method of material analysis. Transactions of the 9th Army Conference on Application of Mathematics and Computing, Minneapolis, USA, pp 57–76

Shi GH, Goodman RE (1989) Generalization of two-dimensional discontinuous deformation analysis for forward modeling. Int J Numer Anal Methods Geomech 13:359–380

Strouboulis T, Babuska I, Copps KL (2000a) The design and analysis of the Generalized Finite Element Method. Comput Methods Appl Mech Eng 181:43–69

Strouboulis T, Copps K, Babuska I (2000b) The generalized finite element method: an example of its implementation and illustration of its performance. Int J Numer Anal Methods Geomech 47:1401–1417

Sulsky D, Chen Z, Schreyer H (1994) A particle method for history-dependent materials. Comput Methods Appl Mech Eng 118:179–196

Sulsky D, Zhou S, Schreyer H (1995) Application of a particle-in-cell method to solid mechanics. Comput Phys Commun 87:236–252

Tang CA, Lin P, Wong RHC, Chau KT (2001) Analysis of crack coalescence in rock-like materials containing three flaws—part II: numerical approach. Int J Rock Mech Min 38:925–939

Tsay RJ, Chiou YJ, Chuang WL (1999) Crack growth prediction by manifold method. J Eng Mech 125:884–990

Vesga LF, Vallejo LE, Lobo-Guerrero S (2008) DEM analysis of the crack propagation in brittle clays under uniaxial compression tests. Int J Numer Anal Methods Geomech 32:1405–1415

Wang YC, Mora P (2008) Modeling wing crack extension: implications for the Ingredients of Discrete Element Model. Pure Appl Geophys 16:609–620

Wang SY, Sloan SW, Sheng DC et al (2014) Numerical study of failure behaviour of pre-cracked rock specimens under conventional triaxial compression. Int J Solids Struct 51:1132–1148

Weibull W (1951) A statistical distribution function of wide applicability. J Appl Mech 18:293–297

Wong RHC, Chau KT, Tang CA, Lin P (2001) Analysis of crack coalescence in rock-like materials containing three flaws—part I: experimental approach. Int J Rock Mech Min 38:909–924

Wong LNY, Einstein HH (2009a) Crack coalescence in molded gypsum and carrara marble: part 1. Macroscopic observations and interpretation. Rock Mech Rock Eng 42:475–511

Wong LNY, Einstein HH (2009b) Crack coalescence in molded gypsum and carrara marble: part 2—microscopic observations and interpretation. Rock Mech Rock Eng 42:513–545

Wu ZJ, Wong LNY (2012) Frictional crack initiation and propagation analysis using the numerical manifold method. Comput Geotech 39:38–53

Yang SQ, Jing HW, Wang SY (2012a) Experimental study on the strength, deformability, failure behaviour and spatial acoustic emission distribution of red sandstone under triaxial compression. Rock Mech Rock Eng 45:583–606

Yang SQ, Yang DS, Jing HW, Li YH, Wang SY (2012b) An experimental study of the fracture coalescence behaviour of brittle sandstone samples containing three fissures. Rock Mech Rock Eng 45:563–582

Yoon J (2007) Application of experimental design and optimization to PFC model calibration in uniaxial compression simulation. Int J Rock Mech Min Sci 44:871–889

York A, Sulsky D, Schreyer H (2000) Fluid-membrane interaction based on the material point method. Int J Numer Methods Eng 48:901–924

Yu MH, Zan YW, Zhao J, Yoshimine M (2002) A unified strength criterion for rock material. Int J Rock Mech Min Sci 39:975–989

Zhang HH, Li LX, An XM, Ma GW (2010) Numerical analysis of 2-D crack propagation problems using the numerical manifold method. Eng Anal Boundary Elem 34:41–50

Zhang XP, Wong LNY (2012) Cracking processes in rock-like material containing a single flaw under uniaxial compression: a numerical study based on parallel bonded-particle model approach. Rock Mech Rock Eng 45:711–737

Zhou XP, Cheng H, Feng YF (2014) An experimental study of crack coalescence behaviour in rock-like materials containing multiple flaws under uniaxial compression. Rock Mech Rock Eng 47:1961–1986

Zhou XP, Bi J, Qian QH (2015a) Numerical simulation of crack growth and coalescence in rock-like materials containing multiple pre-existing flaws. Rock Mech Rock Eng 48(3):1097–1114

Zhou XP, Zhao Y, Qian QH (2015b) A novel meshless numerical method for modeling progressive failure processes of slopes. Eng Geol 192:139–153